CHEMISTRY

UV light–driven late-stage skeletal reorganization to diverse limonoid frameworks: A proof of concept for photobiosynthesis

Jun Wu[1]†, Shi-Jun Li[2]†, Long Jiang[3], Xiao-Chi Ma[4]*, Yu Lan[2,5]*, Li Shen[1]‡*

Late-stage skeletal reorganization (LSSR) is a type of fascinating organic transformation processes in natural product total synthesis. However, few facile and effective LSSR methodologies have hitherto been developed. Here, LSSR of limonoid natural products via photochemical cascades is first reported. Starting from xyloelves A and B, nine distinct limonoid products with five unprecedented scaffolds are generated. The photocascade pathways of these natural products and mechanistic rationale via intramolecular triplet energy transfer are revealed by quantum mechanical calculations. Most notably, ultraviolet light–driven transannular and stereoselective C → C 1,4-acyl migration is first found as a photochemical approach, particularly for LSSR of natural products. This approach holds promise for designing LSSR strategies to access bioactive cage-like molecules. Besides that, our findings provide a clear proof of concept for natural product photobiosynthesis. Xyloelf A, substantially ameliorating concanavalin A–induced liver injury in mice, could be used as a unique molecular template for hepatoprotective drug discovery.

INTRODUCTION

Compared to stepwise synthetic approaches, late-stage diversification of natural products will not only reduce synthetic efforts but also enable access to valuable analogs and derivatives toward identification of therapeutic targets. In recent years, considerable efforts have been devoted to the development of facile and effective methodologies for late-stage diversification of complex natural products. At present, site-selective C—H functionalization approaches, such as the transformation and insertion of site-specific functional groups, are the main strategy, namely, peripheral editing (*1*–*6*). Conversely, skeletal editing, i.e., modification of the underlying molecular skeleton, has limited precedents (*7*). Skeletal reorganization is a type of fascinating skeletal editing organic process, featuring the marked change in bond connectivity of a framework (*8*). Typically, it involves multiple steps of bond cleavage and formation through a concerted mechanism (*9*). Because of synthetic versatility and high atom/step economy, particularly the capability of accessing complex and challenging organic scaffolds from easily accessible feedstocks, skeletal reorganization is of perennial importance in the field of natural product total synthesis (*10*–*12*).

Acyl migration reactions, involved in multiple bioprocesses, have been widely applied in the field of organic synthesis, particularly natural product synthesis. Typical intramolecular acyl migrations include the O ↔ N bidirectional 1,4-acyl migration (Fig. 1A) (*13*), Baker-Venkataraman O → C 1,5-acyl migration (Fig. 1B) (*14*), and transition metal–catalyzed C → C acyl migrations triggered by C—C activation of ketones (Fig. 1C) (*15*). Most notably, transition metal–catalyzed C → C intramolecular acyl migration approaches offer a valuable tool for creating various carbocyclic ring systems. The representative construction process involves cleavage of the acyl-carbon bond and reassembling fragments across an olefin moiety, thereby generating an anticipated carbocyclic ring (Fig. 1C) (*15*). However, the C → C intramolecular 1,4-acyl migration in this pattern is unlikely to occur for the construction of a strained three-membered carbocycle. In recent years, great progress has been achieved in the development of transition metal–catalyzed C → C intramolecular acyl migration reactions. Nevertheless, substrates of these reactions must contain either a strained ketone or a directing group, hampering the application of this methodology (*16*, *17*).

Photochemical transformations, a powerful tool of high value in natural product synthesis, have the potential to access architecturally complex scaffolds. Typical types of photoreactions include various [*n* + 2] photocycloadditions and photochemical rearrangements, such as Norrish-Yang cyclization, meta-photocycloaddition, and oxa-di-π-methane rearrangement (Fig. 1D) (*18*). Notably, ultraviolet (UV) light–induced skeletal rearrangement of the bicyclo[3.2.1]octene moiety resulted in the interconversion between *ent*-kaurane and jungermannenone type of *Isodon* plant diterpenoid skeletons. This late-stage photoradical process might proceed via the C → C intramolecular 1,3-acyl migration of the β, γ-unsaturated ketone moiety (Fig. 1E) (*19*). Undoubtedly, photochemical 1,2-acyl and 1,3-acyl migrations represent a powerful tool to construct various polycyclic carbon backbones of complex natural products (*20*–*23*). To the best of our knowledge, photoinduced C → C intramolecular 1,4-acyl migration has never been reported. Here, we report the natural product–inspired discovery of this photochemical approach and its remarkable capability of creating diverse and complex limonoid scaffolds via late-stage skeletal reorganization, along with photoinduced C → C intramolecular 1,2-acyl migration and photooxidation of the furyl moiety.

[1]Guangdong Key Laboratory of Natural Medicine Research and Development, College of Pharmacy, The First Dongguan Affiliated Hospital, Guangdong Medical University, Dongguan 523808, China. [2]College of Chemistry, Zhengzhou University, Zhengzhou 450001, China. [3]School of Chemistry, Sun Yat-Sen University, Guangzhou 510275, China. [4]Pharmaceutical Research Center, Second Affiliated Hospital, Dalian Medical University, Dalian 116044, China. [5]School of Chemistry and Chemical Engineering, Chongqing Key Laboratory of Theoretical and Computational Chemistry, Chongqing University, Chongqing 400030, China.
†These authors contributed equally to this work.
‡Lead contact.
*Corresponding author. Email: maxc1978@163.com (X.-C.M.); lanyu@cqu.edu.cn (Y.L.); shenli6052@sina.com (L.S.)

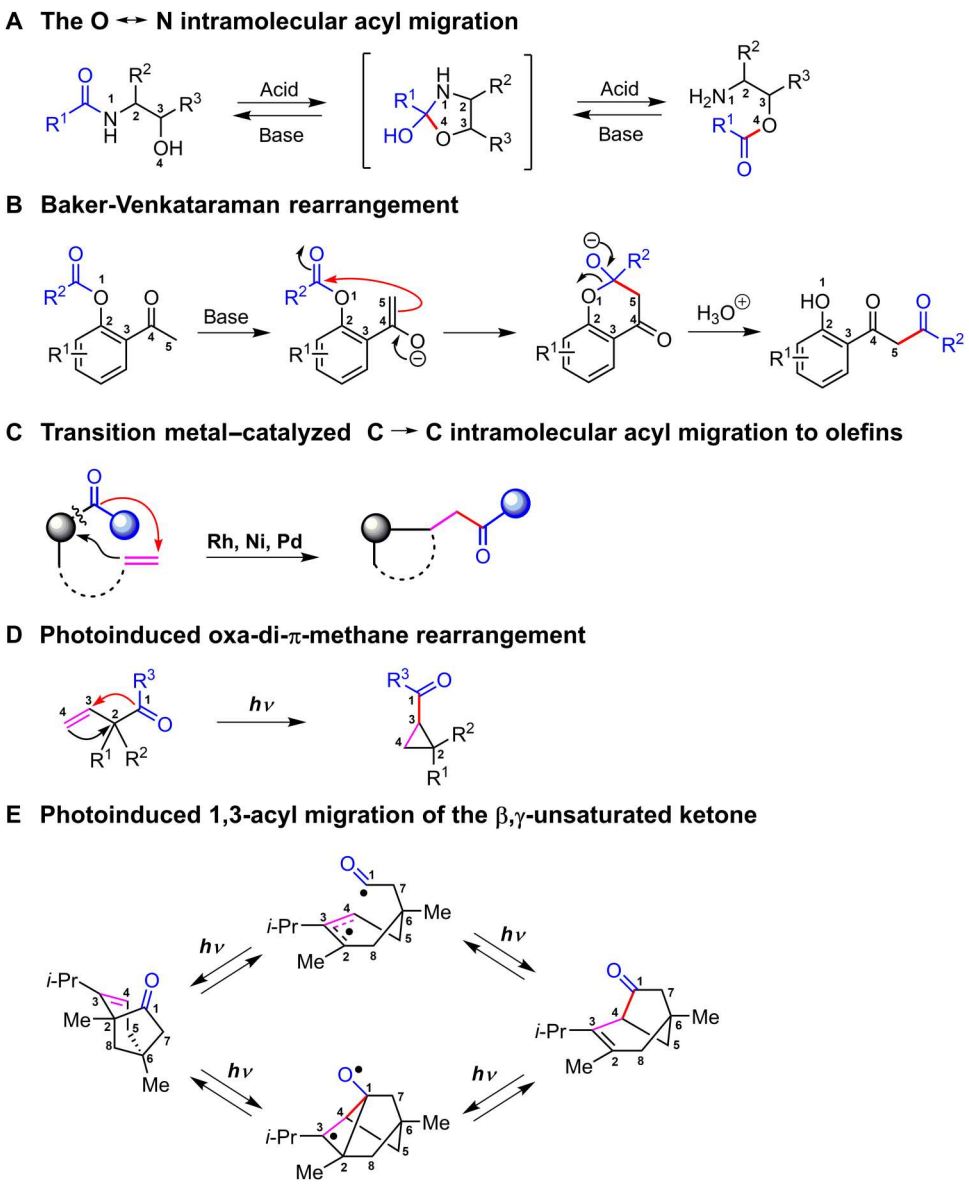

Fig. 1. Background for intramolecular acyl migration reactions. (**A**) O ↔ N 1,4-acyl migration. (**B**) O → C 1,5-acyl migration. (**C**) C → C acyl migrations triggered by C—C activation of ketones. (**D**) C → C 1,2-acyl migration. (**E**) C → C 1,3-acyl migration.

RESULTS

Discovery of limonoid natural products featuring an unprecedented scaffold

Limonoids, highly oxidized natural products with various intriguing tetranortriterpenoid frameworks, have attracted extensive interests for total syntheses in recent years (*24*–*26*). From the perspective of biosynthetic strategy, skeletal rearrangement is deemed to be the crucial step for the generation of diverse limonoid scaffolds (*27*, *28*). However, photoinduced late-stage skeletal rearrangement of limonoids has never been reported. Mangroves of the genus *Xylocarpus* are known to produce fascinating limonoids with architecturally cage-like scaffolds (*29*). Notably, krishnadimer A, the first dimeric limonoid representing an undescribed class of axially chiral nonbiaryl natural products, was isolated and biomimetically synthesized by atroposelective 2,3-dichloro-5,6-dicyanobenzoquinone–mediated dienol-oxidative radical coupling (*30*). During our ongoing projects in search of mangrove natural products with unusual frameworks and remarkable bioactivities, two structurally intriguing limonoids named xyloelves A (**1a**) and B (**1b**) (Fig. 2, A and B), containing a cyclic 2-oxo-30-hemiketal moiety, were obtained from seeds of *Xylocarpus moluccensis*, collected in the tropical mangrove swamp of Trang Province, Thailand. The structures and relative configurations of these limonoids were established by high-resolution electrospray ionization mass spectrometry (HR-ESIMS) and one-dimensional (1D) and 2D nuclear magnetic resonance (NMR) spectroscopic data (fig. S1; see the Supplementary Materials for detailed structural elucidation). Most notably, the constitutions of **1a** and **1b**, each containing an unprecedented cage-like 5/6/6-tricyclic 7-oxatricyclo[4.3.1.$1^{3,10}$]undec-8-ene-5-one nucleus (from C1 to C5, from C8 to C10, C29, and C30), and absolute

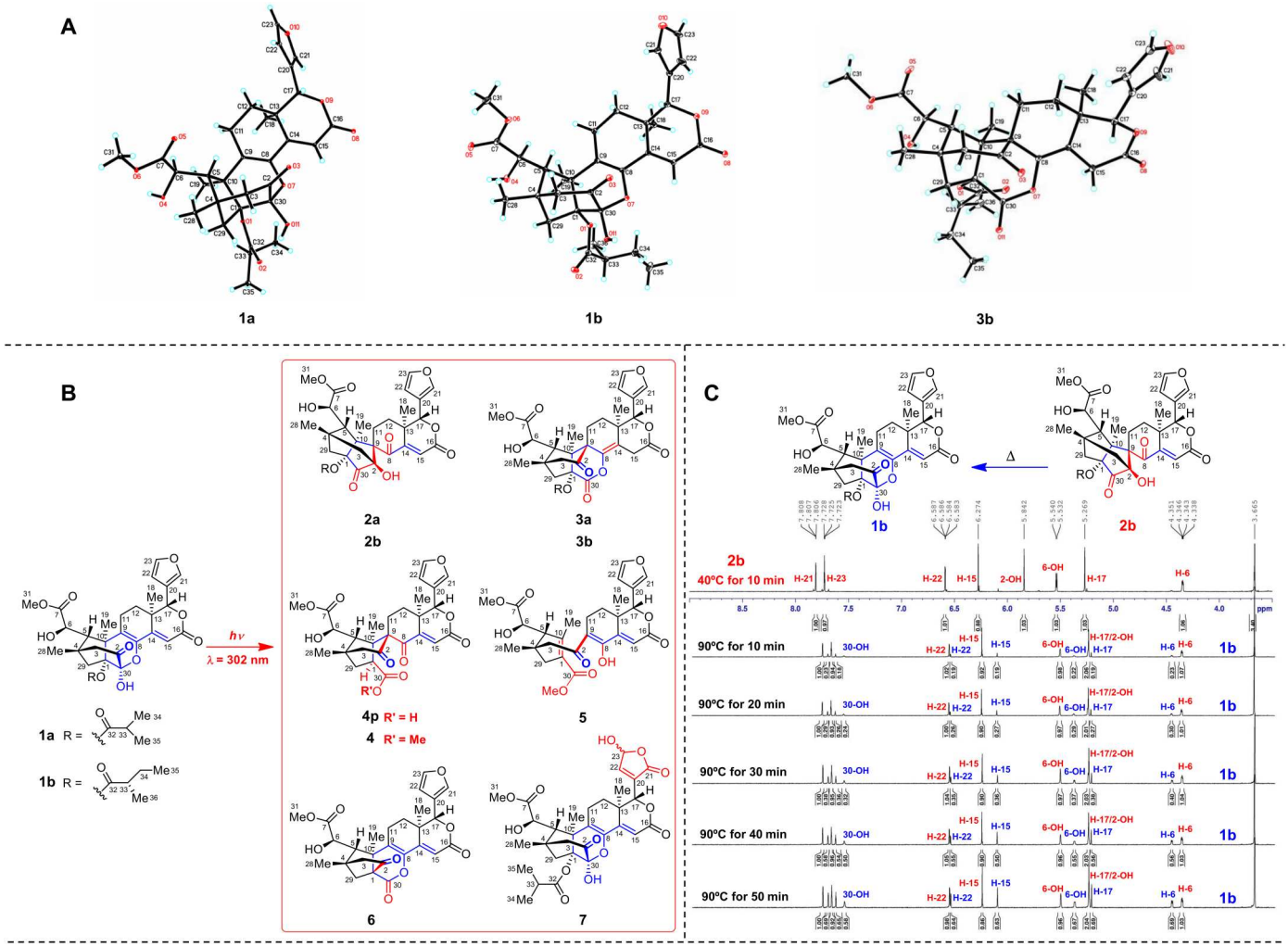

Fig. 2. X-ray crystal structures and photoinduced late-stage skeletal reorganization of limonoid natural products. (**A**) ORTEP plots of x-ray crystal structures of xyloelves A (**1a**) and B (**1b**), as well as **3b**. (**B**) UV light–driven late-stage skeletal reorganization of xyloelves A (**1a**) and B (**1b**) generating photoproducts **2a**, **2b**, **3a**, **3b**, **4p**, and **4** to**7**. (**C**) The thermodynamic retrotransformation of **2b** into xyloelf B (**1b**), monitored by the variable-temperature ^{1}H (600 MHz) NMR spectroscopy analysis in dimethyl sulfoxide (DMSO)–d_6.

configurations of the two compounds, viz., (1*R*,4*S*,5*S*,6*R*,10*S*,13*R*,17*R*,30*R*) and (1*R*,4*S*,5*S*,6*R*,10*S*,13*R*,17*R*,30*R*,33*S*) for **1a** and **1b**, respectively, were unambiguously established by single-crystal x-ray diffraction analyses, conducted with Cu Kα radiation (CCDC 2159544 and 2159461, respectively; Fig. 2A).

Photoinduced late-stage skeletal reorganization of limonoid natural products

Under natural sunlight irradiation with an average intensity of 5000 lux for 16 hours, neat compounds of both xyloelves A (**1a**) and B (**1b**) generated trace amount of **6** (Fig. 2B and table S1), which was produced via the C → C intramolecular 1,2-acyl migration. Upon treatment of **1a** with the same average intensity of sunlight irradiation in acetonitrile for 16 hours, **7** (Fig. 2B and table S1) was obtained in 30.1% isolated yield along with 28.0% of recovered **1a**. When the solvent of the above sunlight irradiation experiment was replaced by dichloromethane, either with or without $FeCl_2$, both **1a** and **1b** were decomposed at last. Treatment of **1a** or **1b** in methanol under average 5000 lux of sunlight irradiation for 1 to 3 hours, **2a**/**3a** or **2b**/**3b** (Fig. 2B and table S1), was observed in pairs as photoproducts but in less than 2.0% yield. Disappointingly, both **1a** and **1b** were ultimately decomposed when the time of sunlight irradiation was extended to 16 hours. To figure out the light wavelength band that really triggered the above photochemical reactions, different light sources, including blue and white light-emitting diode tubes; green, yellow, and red halogen bulbs; and UV 254-, 302-, and 365-nm lamps, were thoroughly investigated (table S1). However, only UV light irradiation at 302 nm notably generated photoproducts. Pleasingly, **2a** and **3a** were simultaneously produced in methanol in 35.3 and 21.1% yields, respectively, when **1a** was irradiated with 302-nm UV light for 1.5 hours. In the same way, **2b** and **3b** were concurrently obtained in 30.2 and 15.1% yields, respectively, when **1b** was chosen as the substrate (table S1). Therefore, UV at 302 nm was selected as the right wavelength for further optimization of photochemical reaction conditions.

Optimization of photochemical reaction conditions and discovery of thermodynamic retrotransformation

As expected, upon 302-nm UV light irradiation at room temperature in different solvents, xyloelves A (**1a**) and B (**1b**) underwent skeletal reorganization to afford eight photoproducts containing five unprecedented limonoid scaffolds, viz., **2a**/**2b**, **3a**/**3b**, **4p**/**4**, **5**, and **6**, and a derivative with a 17-substituted γ(23)-hydroxybutenolide group (**7**) (Fig. 2, B and C). To find the optimal reaction condition, the influence of solvent and UV light irradiation time on photochemical transformation rates of the above substrates, viz., **1a** and **1b**, was scrupulously investigated (tables S2 to S4). As a result, UV light irradiation in the solvent mixture of dimethyl sulfoxide (DMSO) and water (1:1) for 1.0 hour was the optimal reaction condition for the transformation of **1a** into both **2a** and **3a**, isolated in 43.1 and 30.5% yields, respectively. Under the same condition, **2b** and **3b** were obtained from the substrate **1b** in 67.2 and 17.3% isolated yields, respectively. UV light irradiation of **1a** in benzene for 1.5 hours afforded **4p** in 53.1% isolated yield, whereas that in ethyl acetate generated **7** in 26.3% isolated yield (Table 1 and table S2). Upon treatment of **1a** with UV light irradiation in dichloromethane for 0.5 hours, followed by addition of methanol, **4** and **5** were obtained in 13.0 and 10.2% isolated yields, respectively (Table 1 and table S3). The optimal reaction condition for the transformation of **1a** into **6** was in dichloromethane with excess $FeCl_2$ for 1.5 hours. To our delight, **6** was obtained in 33.6% isolated yield (Table 1). Notably, three photosensitizers, viz., methylene blue, rose bengal, and ferroporphyrin, were screened for the improvement of photoinitiation efficiency in the transformation of **1a** into **6**. However, no notable effects were observed at last (table S4).

The thermodynamic retrotransformation of **2a** into **1a** and that of **2b** into **1b**, respectively, was observed when the pure compound **2a** or **2b** was kept away from light in common solvents, such as acetone, acetonitrile, and methanol, at room temperature (normally 20° to 30°C) for several days. To unveil the fast thermodynamic retrotransformation of **2b** into **1b**, variable temperature ^{1}H-NMR spectroscopy analyses were carried out. The photoproduct **2b** was dissolved in DMSO-d_6 in an NMR tube and then heated to 90°C. Every 10 min, the ^{1}H-NMR spectrum was recorded to monitor the retrotransformation rate of **2b** into **1b**, which could be calculated on the basis of the peak area ratio of characteristic proton signals of both compounds, such as H-6 and H-22. As expected, 40% of **2b** was transformed into **1b** after maintaining the temperature of the NMR tube at 90°C for 50.0 min (Fig. 2C).

The structures and relative configurations of all the aforementioned photoproducts, viz., **2a**, **2b**, **3a**, **3b**, **4p**, and **4 to 7**, were established by 1D and 2D NMR spectra, whereas the absolute configurations of these limonoids were determined on the basis of the same absolute configuration of the remained δ-lactone ring-D, i.e., (13*R*,17*R*), occurring in substrates (**1a**/**1b**) and all the photochemical products (figs. S1 and S2) (see the Supplementary Materials for detailed structural elucidation). Most notably, the constitution of **3b** and its absolute configuration, i.e., (1*R*,4*S*,5*S*,6*R*,9*R*,10*S*,13*R*,17*R*,33*S*), were unequivocally established by single-crystal x-ray diffraction analysis, conducted with Cu Kα radiation [Flack parameter of 0.09 (9) and Hooft parameter of 0.08 (7)] (CCDC 2159543; Fig. 2A).

Energy landscape, photocascade pathways, and mechanistic rationale

To gain mechanistic insights into photoinduced late-stage skeletal reorganization of limonoid natural products, density functional theory (DFT) and time-dependent DFT (TD-DFT) calculations at the M06/6-31G(d, p)/the integral equation formalism variant with the solvent dichloromethane [IEFPCM(DCM)] level of theory were performed (*31*–*34*). Xyloelf A (**1a**) was chosen as a model substrate, which could be transformed into five products, viz., **2a**, **3a**, and **4** to **6**, via different photocascade pathways. The thermodynamic retrotransformation of **2a** into **1a** was also confirmed by theoretical calculations (tables S5 to S7).

Two excited singlet states of **1a**, viz., S1 and S2, were found by means of TD-DFT calculations (Fig. 3A). The energy levels of S1 and S2 were well matched with the UV absorption wavelengths of 298 and 313 nm, respectively. Once formed, the singlet diradical S1 could undergo a spin forbidden intersystem crossing process to produce the excited triplet state T1, of which the energy level was 1.89 eV lower than that of S1. The two corresponding singly occupied molecular orbitals (SOMOs), namely, SOMO and SOMO-1, located on the 17-furyl group and the 8,8a-dihydro-1*H*-isochromen-3(7*H*)-one moiety of **1a**, respectively, were obtained by DFT calculations for the excited triplet state T1 (Fig. 3A). Hence, the UV light excitation process could be considered as an intramolecular single-electron transfer. That is to say, the 17-furyl group of **1a** donated one electron to the electron-deficient 8,8a-dihydro-1*H*-isochromen-3(7*H*)-one moiety of the limonoid skeleton, with the aim for further transformations.

In the absence of water, three products could be obtained. Free energy profiles for the transformation of the complex substrate **1a** into three products, viz., **4**, **5**, and **6**, were obtained by DFT calculations (Fig. 3B). The energy of T1 was set to relative zero. Starting from T1, an intramolecular radical-type acyl shift from C30 to C9, with cleavage of the C2—C30 bond and generation of the C2—C9

Table 1. Optimum conditions for photochemical reactions.

Substrate	Solvent	Metal ion	UV at 302 nm, room temperature, (*t*)	Products (isolated yield)
1a	DMSO/H_2O (1:1)	–	1.0 hours	**2a** (43.1%) and **3a** (30.5%)
1b	DMSO/H_2O (1:1)	–	1.0 hours	**2b** (67.2%) and **3b** (17.3%)
1a	Benzene	–	1.5 hours	**4p** (53.1%)
1a	CH_2Cl_2 (add MeOH)	–	0.5 hours	**4** (13.0%) and **5** (10.2%)
1a	CH_2Cl_2	$FeCl_2$	1.5 hours	**6** (33.6%)
1a	EtOAc	–	1.5 hours	**7** (26.3%)

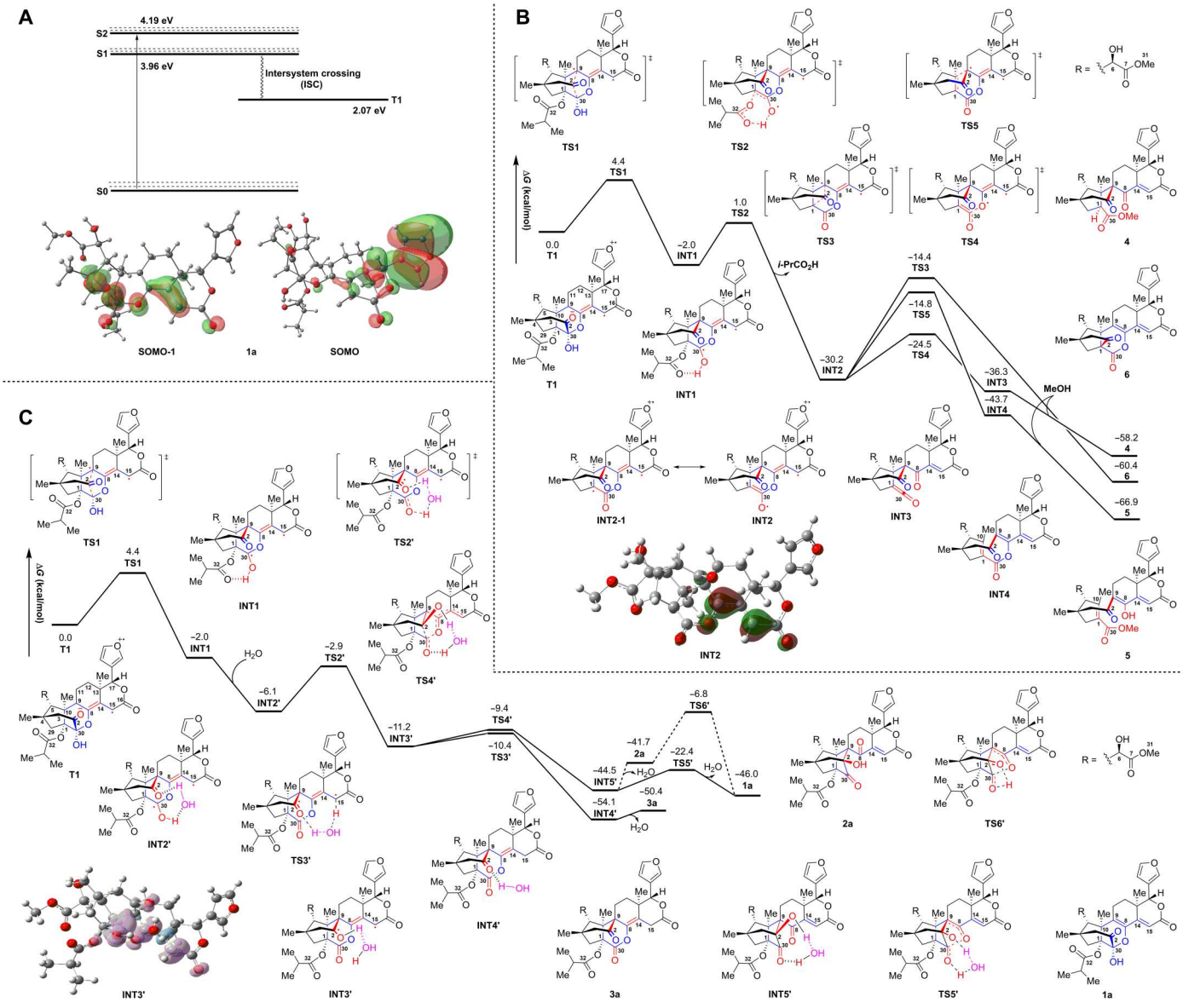

Fig. 3. Energy landscape, computed cascade pathways, and mechanistic rationale for the photochemical transformation of xyloelf A (1a) into five products, along with those for the thermodynamic retrotransformation of into 2a in 1a. (**A**) The diagram for the light process and the SOMOs for the excited triplet state of **1a**. (**B**) Free energy profiles for the photochemical transformation of **1a** into **4**, **5**, and **6** in the absence of water, including the SOMO for the key intermediate **INT2** (the iso value = 0.05 atomic unit). (**C**) Free energy profiles for the photochemical transformation of **1a** into **2a** and **3a** in the presence of water, including the spin density for the key intermediate **INT3**′, along with the free energy profile for the thermodynamic retrotransformation of **2a** into **1a**.

bond, i.e., C → C 1,4-acyl migration, would occur via the transition state TS1 to afford the intermediate INT1. Then, the isobutyryloxy moiety of INT1 could be activated by an intramolecular hydrogen bond between the carbonyl group of the isobutyryloxy moiety and the C30—OH group. Sequent proton transfer via the transition state TS2, overcoming an energy barrier of only 3.0 kcal/mol, would lead to a rapid C—O bond cleavage and the loss of one molecule of isobutyric acid, irreversibly generating the key pyranolate intermediate INT2. Notably, INT2-1 was another essential resonance structure of INT2. On the basis of INT2, three possible pathways might be considered for the generation of diverse photoproducts. The orbital analysis for the SOMO of INT2 revealed the electronic sharing between C8 and C15. Thus, the cleavage of the C30—O ether bond, activated by radicals, would occur via the transition state TS4, surmounting an energy barrier of only 5.7 kcal/mol, to yield the ketene intermediate INT3, of which the energy level was 6.1 kcal/mol lower than that of INT2, indicating a reversible process between INT2 and INT3. Hence, the final photoproducts might be dependent on solvents. In the presence of methanol, **4** was found as the kinetic product for the above reaction.

Alternatively, INT2 could undergo a C9—C10 bond cleavage via the transition state TS5 to afford INT4, of which the energy level was 7.4 kcal/mol lower than that of INT3. The calculated activation barrier for the transformation of INT2 into INT4 was 15.4 kcal/

mol. With the aid of methanol, INT4 could be successfully transformed into the thermodynamic product **5**. In the absence of methanol, however, INT2 would undergo the C → C 1,3-acyl migration via the open-shell singlet transition state TS3 to give **6** as the final product (Fig. 3B).

In the presence of water, either **2a** or **3a** could be provided from the same substrate **1a**. DFT calculations were used to unveil the detailed transformation mechanism. Starting from the common T1 state of **1a**, the formation of INT1 could share with the former pathway via the transition state TS1 with a free energy barrier of 4.4 kcal/mol (Fig. 3C). In presence of the water, the intermediate INT2′ could be obtained with bridged hydrogen bonds of carbonyl and hydroxyl moieties in the INT1 with an exothermic process of 4.1 kcal/mol. Subsequently, a water-assisted intramolecular hydrogen shift could occur and then resulted in a rearrangement of the hydroxyl alkyl radical in the intermediate INT3′ via the transition state TS2′ with a free energy barrier of 3.2 kcal/mol. In the triplet intermediate INT3′, the spin density was majorly shared by C2, C15, and C30. Therefore, either water-assisted hydrogen atom transfer to C15 or radical-type substitution onto C30 was possible, leading to two possible pathways for the generation of different products. The spin density on C15 exhibited the hydrogen-acceptor character, where C15 could achieve a hydrogen atom transfer from the hydroxyl alkyl moiety. In the presence of a water bridge, this hydrogen atom transfer could occur via the transition state TS3′ with a free energy barrier of only 0.8 kcal/mol. After releasing a molecule of water, the product **3a** could be formed by this pathway. Alternatively, TS4′ could be considered as an initial radical addition of C2 onto the lactone moiety, accompanied by the cleavage of C30—O ether bond. After releasing a molecule of water, another product **2a** would be yielded. The calculated relative free energy of the transition state TS4′ was only 1.0 kcal/mol higher than that of TS3′. Therefore, both **2a** and **3a** could be experimentally observed. Once **2a** was formed, a water-assisted retro-Michael addition could occur via the transition state TS5′, leading to the cleavage of the C2—C9 bond. Meanwhile, the water bridge resulted in the acetalation for the formation of the C30—O ether bond. The above synergetic process lastly afforded the substrate **1a**, which was 4.3 kcal/mol more stable than **2a**. Notably, the direct thermodynamic retrotransformation from **2a** into **1a** was hard to overcome an energy barrier of 34.9 kcal/mol via the transition state TS6′, indicating the pivotal role of the water bridge for the above intramolecular proton transfer.

Identification of xyloelf A as an agonist of human pregnane X receptor

Nowadays, human pregnane X receptor (hPXR) is regarded as the key nuclear receptor target for the treatment of cholestasis and liver injury diseases (*35*). To find promising drug leads for treating these metabolic diseases, xyloelves A (**1a**) and B (**1b**) and their LiOH hydrolysate **1c** (fig. S1), as well as all the photoproducts, viz., **2a**, **2b**, **3a**, **3b**, **4p**, and **4**–**7** (Fig. 2B), were screened for agonistic effects on hPXR by the luciferase assay based on the hPXR-luc reporter in human embryonic kidney (HEK) 293T cells (*36*). Rifampicin (RIF) was used as the positive control at the concentration of 10.0 μM. To our delight, **1a** ameliorated a potent agonistic effect on hPXR in a dose-dependent manner within the concentration range of 10.0 nM to 10.0 μM (Fig. 4A), whereas all the other compounds showed relatively weak activation effects (fig. S3). Multidrug resistance gene 1 (MDR1) and cytochrome P450 3A4 (CYP3A4) were recognized as the well-documented downstream targets of hPXR. To further confirm the activation effects of **1a** toward these targets, the mRNA and protein levels of MDR1 and CYP3A4 were analyzed by Western blot after the treatment of human hepatic carcinoma (HepG2) cells with **1a** for 24 hours. RIF was used again as the positive control. **1a** remarkably up-regulated the mRNA (fig. S4A) and protein (Fig. 4B) levels of MDR1 and CYP3A4 in HepG2 cells, particularly within the concentration range of 100.0 nM to 10.0 μM.

To elucidate the underlying mechanism for the agonistic effect of **1a** on hPXR, molecular docking study was performed on the basis of the crystal structure of the ligand **1a** and the receptor hPXR (*36*–*38*). The defined hPXR_**1a** interaction model, obtained from the residual energy–based stable election protocol, was well-converged to afford an ideal equilibrium state with the root mean square deviation value of less than 2 Å in molecular dynamics (MD) study (fig. S4B). As a result, **1a** could bind to the ligand-binding domain (LBD) of hPXR and then form a rather stable complex (Fig. 4C). The interaction scenario of **1a** with the LBD of hPXR was further analyzed. The energy decomposition analysis unveiled that 11 residues, viz., Leu^{240}, Met^{243}, Ser^{247} (S247), Phe^{281}, Cys^{284}, Phe^{288} (F288), Trp^{299} (W299), Tyr^{306}, Met^{323}, His^{407} (H407), and Leu^{411}, remarkably contributed to the ligand-receptor interaction that helps to stabilize the binding (Fig. 4C and fig. S4C). Most notably, the residue S247 formed a stable hydrogen bond with the 7-keto group of **1a**, whereas residues F288 and W299 participated largely in the electrostatic interactions with the 17-furyl ring of **1a**. The residue H407, exhibiting an unusual protonation state, should be a preferred center for the polar interactions with the Me-19 and 1-*O*-isobutyryl group of **1a**. To further validate the molecular interaction between **1a** and the LBD of hPXR, four key residues—S247, F288, W299, and H407—were selected and mutated to S247A, F288D, W299D, and H407D, respectively. As a result, these mutations, particularly S247A, F288D, and H407D, significantly diminished the response of hPXR to **1a** (Fig. 4C). Together, we may conclude that **1a** is a potent hPXR agonist targeting the LBD of hPXR.

Xyloelf A ameliorates concanavalin A–induced liver injury in mice

The protective effects of xyloelf A (**1a**) on concanavalin A (Con A)–induced liver injury in mice were thoroughly investigated. Before the treatment with intravenous Con A at a sublethal dose (15.0 mg/kg), two groups of mice were intraperitoneally pretreated daily with **1a** at a dose of 20.0 or 40.0 mg/kg for 3 days (Fig. 4D and fig. S5A). On the fourth day, after the treatment of Con A for 10 hours, mice were euthanized. Then, mice liver tissues and blood samples were collected. The Con A–treated mice resulted in notable liver injury. As expected, the pretreatment of **1a** remarkably reduced Con A–induced liver damage in mice (fig. S5A). In line with these findings, livers of mice only treated with Con A exhibited typical damage featuring focal necrosis, which could be markedly reduced by the pretreatment of **1a** (Fig. 4D). As shown in Fig. 5A, the plasmatic levels of alanine aminotransferase (ALT) and aspartate aminotransferase (AST) in mice could be up-regulated by Con A. However, the pretreatment of **1a** noticeably decreased the plasmatic levels of the above enzymes. Terminal deoxynucleotidyl transferase-mediated deoxyuridine triphosphate nick end labeling

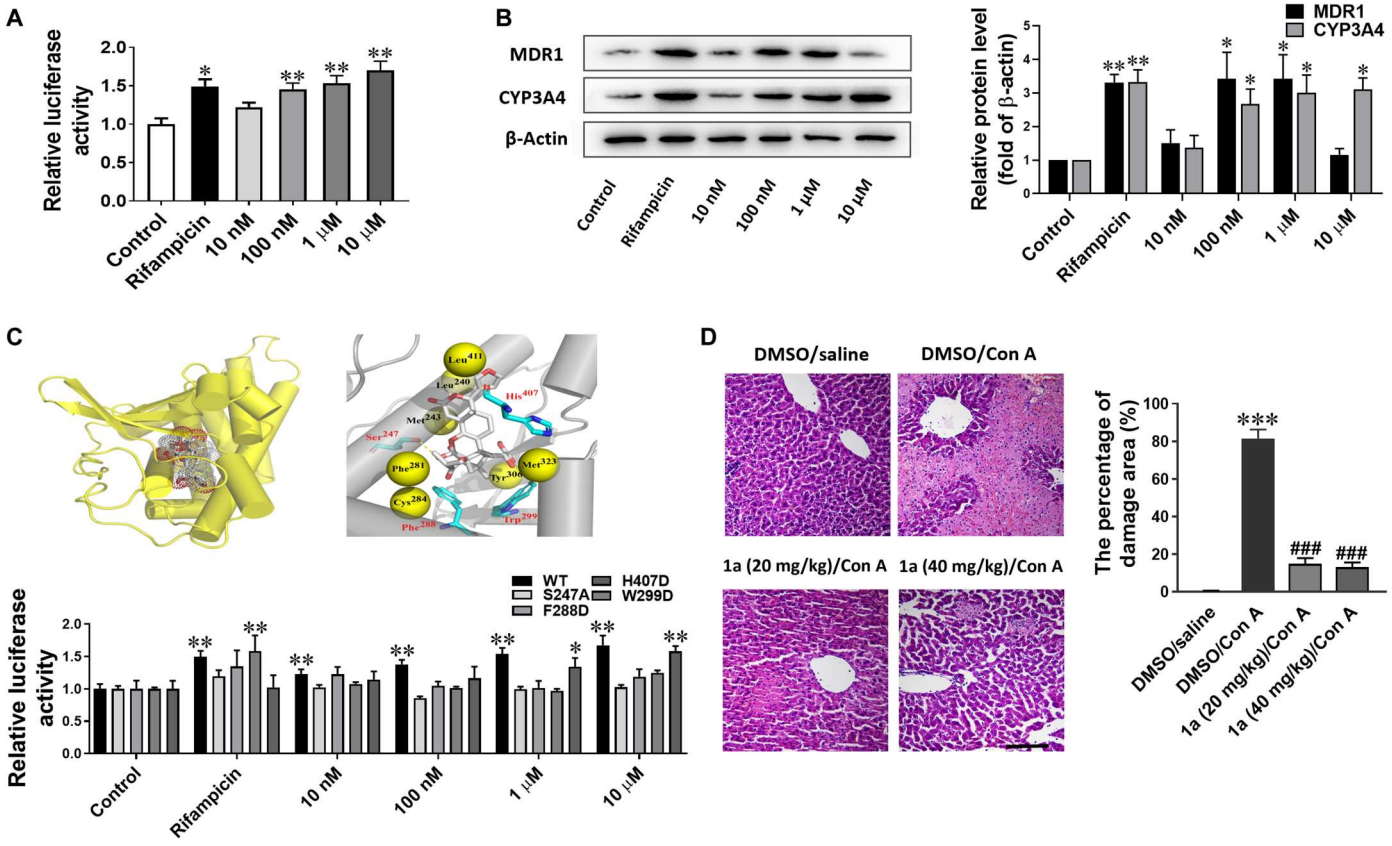

Fig. 4. Xyloelf A (1a), identified as an agonist of hPXR, ameliorates Con A–induced liver injury in mice. (**A**) Activation effects of **1a** on hPXR at the concentrations of 10.0 and 100.0 nM and 1.0 and 10.0 μM, assessed by the PXR-luciferase reporter assay in human embryonic kidney (HEK) 293T cells. Data represent the means ± SD, $n = 4$ to 6 for each group. *$P < 0.05$ and **$P < 0.01$ compared to the control group. RIF was used as the positive control at the concentration of 10.0 μM. (**B**) Western blot analysis revealing the significant up-regulation of the protein levels of MDR1 and CYP3A4 after the treatment of **1a** in HepG2 cells for 24 hours. Data represent the means ± SD, $n = 3$ for each group. *$P < 0.05$ and **$P < 0.01$ compared to the corresponding control group. (**C**) Top: Molecular docking unveiling the 3D structure binding of **1a** with the ligand-binding domain (LBD) of hPXR. Bottom: Site mutagenesis analysis revealing activation effects of **1a** on the wild-type (WT) and mutant hPXR. Data represent the means ± SD, $n = 4$ to 6 for each group. *$P < 0.05$ and **$P < 0.01$ compared to the corresponding control group. (**D**) Left: Representative images showing hematoxylin and eosin staining in liver sections after mice were treated with or without concanavalin A (Con A) and **1a**. Right: Statistical analysis of liver damage area after mice were treated with or without Con A and **1a**. Data represent the means ± SD, $n = 4$ for each group. ***$P < 0.001$ compared to the DMSO/saline group; ###$P < 0.001$ compared to the DMSO/Con A group.

(TUNEL) assay unveiled that both doses of **1a** decreased the number of apoptotic liver cells, thereby indicating the potent anti-apoptotic effect of **1a** on Con A–induced liver injury (fig. S5B). Western blot analysis demonstrated that levels of antiapoptotic Bcl-2, proapoptotic Bax, cleaved caspase-3, and cleaved caspase-9 were reversed by the pretreatment of **1a** (fig. S5C Most notably, the quantitative real-time polymerase chain reaction (qPCR) results revealed that the pretreatment of **1a** markedly repressed the Con A up-regulated mRNA levels of proinflammatory cytokines, viz., tumor necrosis factor–α (TNFα), interleukin-1 (IL-1), interleukin-2 (IL-2), interleukin-6 (IL-6), C-C motif chemokine 2 (CCL2), > C-X-C motif chemokine 2 (CXCL2), Fas antigen ligand (FASL), intercellular adhesion molecule–1 (ICAM-1), and interferon-γ (IFN-γ) (Fig. 5B). In addition, Con A–up-regulated levels of Beclin-1, microtuble-associated proteins 1A/1B light chain 3 (LC3 I/II), inducible nitric oxide synthase, and p65, regarded as important factors in processes of autophagy and inflammatory, were markedly reversed by the pretreatment of **1a** (fig. S5, D and E). In summary, **1a** substantially ameliorated Con A–induced liver injury in mice. It could be used as a lead compound for hepatoprotective drug discovery.

DISCUSSION

Historically, high-energy UV light–driven photochemical reactions have been applied in organic synthesis for over a century (*18*). On our earth, the tropics and plateaus are the areas with the strongest UV radiation. As a result of long-term adaptation to natural environment, living organisms, particularly animals and plants in the above areas might use UV light–driven photochemical reactions in natural product biosynthetic processes, especially late-stage skeletal editing of polycyclic terpenoids. From the standpoint of biosynthesis, intricarene (*39*) and bielschowskysin (*40*), highly oxidized and congested diterpenoids isolated from the Caribbean coral *Pseudopterogorgia kallos*, are furanobutenolide-derived polycyclic cembranoids (*41*). Starting from the biosynthetic precursor, bipinnatin J, a common macrocyclic furanocembranoid of corals, photochemical synthesis of intricarene, involving a magic step of UV light–driven skeletal rearrangement, was successfully achieved, although

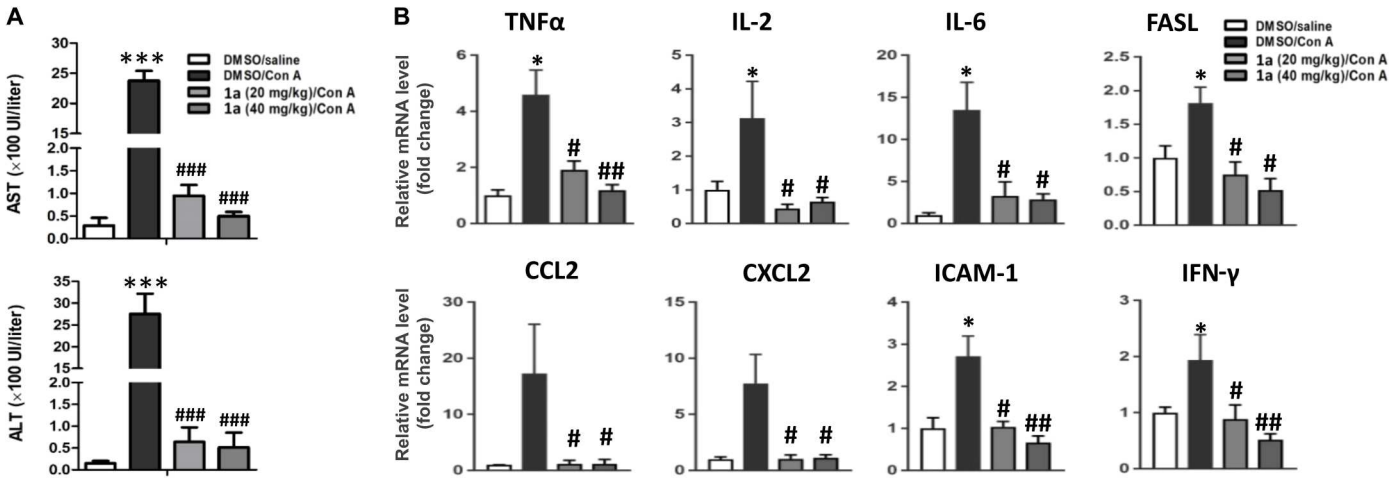

Fig. 5. Xyloelf A (1a) ameliorates Con A–induced liver injury in mice (continued). (**A**) Plasmatic levels of ALT and AST after mice were treated with or without Con A and **1a**. Data represent the means ± SD, $n = 4$ for each group. ***$P < 0.001$ compared to the DMSO/saline group; ###$P < 0.001$ compared to the DMSO/Con A group. UI, Unit International. (**B**) mRNA levels of liver proinflammatory cytokines, including TNFα, IL-1, IL-2, IL-6, FASL, CCL2, CXCL2, ICAM-1, and IFN-γ, after mice were treated with or without Con A and **1a**. Data represent the means ± SD, $n = 4$ for each group. *$P < 0.05$ compared to the DMSO/saline group; #$P < 0.05$ and ##$P < 0.01$ compared to the DMSO/Con A group.

the 2-OH group and furan ring of bipinnatin J had to be methylated and oxidized, respectively, before UV light irradiation. The underlying mechanistic scenario was revealed by quantum chemical calculations as the continuous photocascade process via a series of triplet intermediates (*42*). Note that bielschowskysin was ultimately synthesized from late-stage skeletal rearrangement of the same precursor, bipinnatin J. The whole process, however, included multiple steps, viz., UV light–induced Entgegen/Zusammen (*E*/*Z*) isomerization, epoxidation, dearomatization, and transannular [2 + 2] photocycloaddition (*43*). In addition, sunlight-induced 1,3-allyl shift of bipinnatin J afforded the pseudopterane-type diterpenoid kallolide A (*44*). Undoubtedly, UV light–driven late-stage skeletal rearrangement ought to play a pivotal role in the biosynthesis of furanobutenolide-derived coral cembranoids.

Mangroves of the genus *Xylocarpus*, belonging to the plant family Meliaceae, are widely distributed across tropical and subtropical estuarine swamps, from southern Africa to west and central Pacific Ocean. Limonoids are the main type of natural products of these mangroves. Our phytochemical investigations over the last 20 years revealed that environmental factors, such as temperature, salinity, and light, should play the leading role for these mangroves to produce unique and diverse limonoids, whereas the genetic background might be secondary (*29*, *30*, *45*, *46*). In this study, experimental and computational investigations unveil late-stage skeletal reorganization of Thai *Xylocarpus* mangrove limonoids, enabled by UV light–driven photochemical cascades. Our discovery combined with the previously reported UV light–driven late-stage skeletal rearrangement of Chinese *Isodon* plant diterpenoids (*19*) and Caribbean coral furanobutenolide-derived cembranoids (*42*) constitutes a chain of evidence for a previously unimaginable concept, here termed as natural product photobiosynthesis—in other words, living organisms, particularly tropical and plateau animals and plants, have the capability of synthesizing natural products by direct utilization of sunlight energy, the ultimate driving force of biosynthesis on the earth, instead of enzymes in the body. Incontrovertibly, photobiosynthesis is of great importance in natural product biosynthesis, although this concept has been unappreciated and undervalued all along. It is not only an essential part of natural product biosynthesis but also a necessary supplement to multifarious enzyme-catalyzed biosynthetic pathways, which might be correspondingly termed enzymobiosynthesis.

In the past decade, visible light photoredox catalysis has become an immensely valuable tool in natural product synthesis. With the aid of this photocatalytic strategy, the construction of structurally elaborate natural products has been successfully achieved. However, most synthetic processes of these natural products only use one step of visible light photoredox catalysis. In general, organic compounds do not absorb visible light. Fundamentally, visible light photoredox catalysis is not advantageous to the skeletal reorganization/rearrangement of natural products (*47*, *48*).

In summary, two limonoid natural products, named xyloelves A and B, each containing a cage-like 5/6/6-tricyclic 7-oxatricyclo[4.3.1.1^{3,10}]undec-8-ene-5-one nucleus and a cyclic 2-oxo-30-hemiketal moiety, are identified from seeds of a Thai tropical mangrove *X. moluccensis*. UV light–driven late-stage diversification of xyloelves A and B generates nine distinct products with five unprecedented limonoid scaffolds. This is the first report that photoinduced late-stage skeletal reorganization of natural products has been observed to afford a collective of products with diverse and stereospecific frameworks. Notably, UV light–driven transannular and stereoselective C → C 1,4-acyl migration is first unveiled as a promising photochemical approach, particularly for late-stage skeletal reorganization of natural products. The photocascade pathways of the above limonoid products and mechanistic rationale via intramolecular triplet energy transfer are unraveled by quantum mechanical calculations. The role of water not only associates with the substrate through hydrogen bonds, thus remarkably reducing the activation energy and triggering the proton transfer under UV light irradiation, but also maintains the molecular integrity of natural products. These results might be considered as the long-term stress response of the mangrove *X. moluccensis* to the Thai

estuarine environment of tropical intertidal zones. The skeletal reorganization divergence of xyloelves A and B for selective entry to different scaffolds is summarized. Pivotal and mild photochemical cascades in this study hold promise for further extensive applications in the field of organic synthesis, particularly natural product total synthesis. Most notably, our findings provide a tangible proof for the inspiring concept—natural product photobiosynthesis, often resulting in late-stage skeletal editing of complex polycyclic terpenoid natural products. Evidently, photobiosynthesis is essentially complimentary to the traditional enzymobiosynthesis. In addition, xyloelf A exhibits a marked agonistic effect on hPXR in a dose-dependent manner. As a valuable agonist targeting the LBD of hPXR, it substantially ameliorates Con A–induced liver injury in mice. Accordingly, xyloelf A can be used as a unique molecular template in medicinal chemistry for hepatoprotective drug discovery. This work not only opens a door to the future for natural product–inspired discovery of unknown and exciting photochemistry but also creates a facile and effective skeletal editing methodology to access challenging and polycyclic organic molecules with complex, diverse, and even bioactive scaffolds.

MATERIALS AND METHODS

Experimental design

The overall workflow has the following steps: (i) collection of mangrove seeds; (ii) extraction, isolation, and structure elucidation of undescribed natural products, viz., xyloelves A (**1a**) and B (**1b**); (iii) alkaline hydrolysis of the above natural products to afford **1c**; (iv) photochemical preparation of nine compounds, viz., **2a**, **2b**, **3a**, **3b**, **4p**, **4**, **5**, **6**, and **7** from the above natural products; (v) optimization of photochemical reaction conditions; (vi) structure elucidation of the above photochemical reaction products; (vii) DFT and TD-DFT theoretical calculations; (viii) various bioassays; (ix) statistical analysis; and (x) protein docking analysis.

General experimental procedures

HR-ESIMS data were obtained on a Bruker maXis ESI quadruple time-of-flight mass spectrometer in the positive-ion mode. 1D and 2D NMR spectra were measured on a Bruker AV 400-, 600-, or 700-MHz NMR spectrometer. UV spectra were recorded on a GENESYS 10S UV-visible spectrophotometer (Thermo Fisher Scientific), and optical rotations were determined on an MCP500 modular circular polarimeter (Anton Paar GmbH) with a 0.5-cm cell at 25°C. Electronic circular dichroism spectra were recorded on a Jasco J-810 spectropolarimeter with a 1.0-mm cell at room temperature. High-performance liquid chromatography (HPLC) was performed on a Waters 2535 pump equipped with a 2998 photodiode array detector and YMC C_{18} reversed-phase columns (250-mm by 4.6-mm internal diameter, 5 μm, for analysis; 250-mm by 10-mm internal diameter, 5 μm, for preparation; YMC, Kyoto, Japan). For column chromatography, silica gel (100 to 200 mesh) (Qingdao Mar. Chem. Ind. Co. Ltd.) and C_{18} reversed-phase silica gel (12 nm, 50 μm; ODS-A-HG, YMC, Japan) were used. Quartz 5-mm NMR tubes were chosen for photochemical reactions. A UV analyzer (ZF1-II), containing ten UV lamps (each 6 W) and a visible light lamp (60 W), was purchased from Shanghai Jiapeng Technology Co. Ltd. Three UV wavelengths, viz., 254, 302, and 365 nm, could be selected. The distance between the liquid surface of samples inside NMR tubes and the UV light source was about 20.0 cm. The averaged intensity of UV irradiance was about 20.0 μW/cm^2. RIF was purchased from Sigma-Aldrich (St. Louis, MO, USA). All chemicals used in bioassay were dissolved in DMSO.

Mangrove material

Seeds of the mangrove, *X. moluccensis*, were collected in June 2013 from mangrove swamps of the Trang Province, Thailand, with the help of P. Pedpradab (Rajamangala University of Technology Srivijaya, Trang Province, Thailand). The identification of the mangrove was performed by one of the authors (J.W.). Voucher sample (no. ThaiXM-03) is maintained in the Guangdong Key Laboratory of Natural Medicine Research and Development, Guangdong Medical University.

Extraction and isolation

The air-dried seeds (10.0 kg) were powdered and extracted with 95% (v/v) EtOH (5× 20 liters) at room temperature to afford the resulting extract (680.0 g), which was partitioned between EtOAc and water to provide an EtOAc portion (296.0 g). The EtOAc portion was chromatographed on a silica gel column (120-cm by 10-cm internal diameter), eluted with a gradient mixture of $CHCl_3$/MeOH (100:0 to 5:1), to yield 160 fractions (*49*–*52*). Fractions 29 to 40 (110.7 g) were combined and further separated by an RP-18 column (100.0-cm by 5.0-cm internal diameter), eluted with a gradient mixture of acetone/H_2O (50:50 to 100:0), to yield 175 subfractions, among which subfractions 116 to 131 (2.20 g) were combined and purified by preparative HPLC (250-mm by 10-mm internal diameter; MeCN/H_2O, 38:62; YMC-Pack) to afford xyloelf A (**1a**) (320.0 mg, retention time (t_R) = 38.5 min), whereas subfractions 157 to 175 (1.20 g) were combined and purified by preparative HPLC (250-mm by 10-mm internal diameter; MeCN/H_2O, 37:63; YMC-Pack) to afford xyloelf B (**1b**) (120.0 mg, t_R = 52.7 min).

Alkaline hydrolysis of xyloelves A (1a) and B (1b) to afford 1c

A portion of **1a** (2.0 mg, 0.0034 mmol) or **1b** (2.0 mg, 0.0033 mmol) was dissolved in the mixture of methanol and water (2:1, 3.0 ml). A 15.0 eq of LiOH were carefully added and stirred at room temperature overnight until the completion of the reaction (monitored by thin-layer chromatography, i.e., TLC). Then, the solution was neutralized with glacial acetic acid and concentrated under reduced pressure. The resulting residue was dissolved in methanol, whereas the insoluble matter was precipitated by centrifugation. The supernatant was further purified by HPLC (250-mm by 4.6-mm internal diameter; MeCN/H_2O, 40:60; YMC-Pack) to afford compound **1c** (1.6 mg, 0.0031 mM, t_R = 6.3 min).

Photochemical preparation of compounds 2a, 2b, 3a, 3b, 4p, 4, 5, 6, and 7

Oven-dried quartz NMR tubes were each charged with **1a** (0.5 mg, 0.85 μmol) or **1b** (0.5 mg, 0.825 μmol) that was dissolved in 0.6 ml of different solvents. The mixtures were then irradiated with UV light, visible light, halogen light, or sunlight at room temperature. The reactions were monitored by TLC. The last reaction mixtures were concentrated under reduced pressure and analyzed by HPLC. The conversion rates were determined by the integral area ratios of the resulting chromatographic peaks observed at UV 210 nm (UV λ_{max} of the 17-furyl ring within the structure of limonoid) or by isolated yields.

Computational detail

All the theoretical calculations in the study were performed using Gaussian 16 program package (*31*). The M06-2X method with the 6-31G(d, p) basis set was used for the optimization in the solvent phase (*32*). The solvent effect was considered by using the polarizable continuum model using the integral equation formalism variant (IEFPCM) with the solvent dichloromethane (DCM). The harmonic vibrational frequency calculations were performed at the same level to confirm the local minima and transition state. All the optimized stationary points had been identified as minima (zero imaginary frequencies) and transition states (one imaginary frequency) via the vibrational analysis. TD-DFT studies were conducted at same level within the adiabatic approximation to predict the excitation energies (*33*, *34*).

Cell culture

The HEK cell line HEK293T and hepatic carcinoma cell line HepG2 were cultured in Dulbecco's modified Eagle's medium containing 10% fetal bovine serum. Cells were all placed in an incubator at 37°C and maintained in a humidified atmosphere containing 5% CO_2.

Luciferase assay

hPXR expression vector and hPXR reporter (CYP3A4XREM-luciferase) were provided by C. Zhou at University of Kentucky (*53*). HEK293T cells were cultured and transiently transfected with hPXR expression vector and hPXR reporter by using the Lipofectamine 3000 Transfection Reagent (Invitrogen, Carlsbad, CA, USA). The null Renilla luciferase plasmid was used as an internal control. After 24 hours, the cells were treated with compounds **1a**, **1b**, and **1c** at different concentrations. DMSO (0.1%) was used as vehicle. RIF (10 μM) was used as the positive control for the activation of hPXR. The cells were then harvested for the determination of luciferase activity using the Dual-Luciferase Reporter Assay Kit (E1960, Promega, Madison, WI, USA). The fluorescence intensity was measured using a luminometer (Turner BioSystems, USA). The results were normalized by Renilla luciferase activity.

Construction of mouse Con A–induced liver injury model

All animal experiments in this study were conformed to international guidelines for animal usage in research. All protocols for this animal study conformed to the guide for the care and use of laboratory animals. All animal experiments were performed in accordance with guidelines approved by the Ethics Committee of Dalian Medical University (AEE19047). *Pxr* knockout ($Pxr^{-/-}$) mice on C57BL/6N genetic background, generated by deleting exons of Nr1i2 (17,138 base pairs), were provided by Cyagen Biosciences (Suzhou, China). All comparisons used littermate $Pxr^{-/-}$ and $Pxr^{+/+}$ mice that were generated from $Pxr^{+/-}$ breeders. The wild-type and $Pxr^{-/-}$ mice used in the study were housed in a standard specific pathogen–free environment. Male wild-type C57BL/6J mice (8 weeks old) were obtained from the Beijing Vital River Laboratory Animal Technology Co. (Beijing, China), housed in a temperature of 22° ± 1°C with a 12-hour light-dark cycle (6:00 to 18:00) and 65 ± 5% humidity, and fed with an ad libitum diet. Mice were randomly divided into four groups with four to six animals each: DMSO/saline, DMSO/Con A, **1a** (20 mg/kg)/Con A, and **1a** (40 mg/kg)/Con A. Two groups of mice, viz., **1a** (20 mg/kg)/Con A and **1a** (40 mg/kg)/Con A, were intraperitoneally pretreated daily with **1a** for 3 days, whereas the additional two groups, viz., DMSO/saline and DMSO/Con A, were administrated with equal volume of DMSO for 3 days. On the fourth day, three groups of mice, viz., DMSO/con A, **1a** (20 mg/kg)/Con A, and **1a** (40 mg/kg)/Con A, were intravenously administrated with Con A (15 mg/kg), whereas the other group, i.e., DMSO/saline, was intravenously treated with saline. Ten hours after administration, mice were euthanized. At the time of euthanasia, liver tissues and blood samples were collected for further bioassays.

Hepatic pathological assessments and measurements of plasma samples

The liver tissues were formalin-fixed and paraffin-embedded. The sections were stained with hematoxylin and eosin according to the standard protocols. The serum and urine samples were collected and stored at −80°C. Serum AST (C010-2) and ALT (C009-2) were measured by using commercial kits purchased from Jiancheng Bioengineering Institute (Nanjing, China).

RNA isolation and qPCR

Mice liver samples (100 mg each) were collected for the extraction of RNA by TRIzol reagent (Invitrogen, Carlsbad, CA, USA). The quantity and purity of the RNA extraction samples were determined by measuring the sample absorbance at 260/280 nm using a NanoDrop spectrophotometer (Thermo Fisher Scientific, Waltham, MA, USA). Two micrograms of the total RNA from each sample was used for cDNA preparation by the reverse transcriptase (AT-341-01, Tiangen Biotech, Beijing, China). Then, cDNA was used as the template for the qPCR reaction using an Applied Biosystems 7500 Real-time PCR System (Thermo Fisher Scientific, Waltham, MA, USA) with TransStart Tip Green qPCR SuperMix (Transgen, Beijing, China). β-Actin was used as the internal control. Primers used in this study were designed by the Software Oligo 6.0 (Marrone Bio Innovations (MBI) Inc., Colorado, USA) and listed in table S5.

Western blot

Tissues were dissolved in radioimmunoprecipitation assay lysis buffer (Merck, Darmstadt, Germany) with protease inhibitor and phenylmethylsulfonyl fluoride. Protein concentrations were measured by bicinchoninic acid assay kit (Thermo Fisher Scientific, Waltham, MA, USA). Samples were denatured by heating the mixture of the lysates and loading buffer for 10 min at 95°C. Thirty micrograms of total protein were separated by 10% SDS–polyacrylamide gel electrophoresis and transferred onto a nitrocellulose membrane (Thermo Fisher Scientific, Waltham, MA, USA). Membranes were then blocked with 10% (w/v) skim milk and subsequently incubated with primary antibodies overnight at 4°C. Horseradish peroxidase–conjugated secondary antibodies were added for 1.0 hour after washing, followed by signal detection on a Tanon 5200 system (Tanon, Shanghai, China). The ImageJ software (Rawak Software Inc., Germany) was selected for protein expression level quantification and densitometric analysis.

TUNEL assay

The TUNEL assay was applied using an in situ cell death detection kit (Roche, Mannheim, Germany) according to the manufacturer's protocol. Briefly, the formalin-fixed sections were deparaffinized before rehydration with a series of decreasing concentrations of ethanol. After washing with 0.85% NaCl and phosphate-buffered

saline (PBS), the sections were fixed with 4% formaldehyde for 15 min. The sections were covered with proteinase K solution for 15 min and then TUNEL reaction mixture for 1.0 hour. After terminating the reaction by three washes with PBS, the sections were incubated in the Converter Peroxidase (POD) at 37°C for 30 min and then stained with diaminobenzidine to detect apoptotic cells. The sections were examined and photographed using a bright-field/fluorescence microscope (Leica, Wetzlar, Germany). Apoptotic cells were quantified by the ImageJ software (Rawak Software Inc., Stuttgart, Germany).

Statistical analysis

Statistical analyses were performed using the GraphPad Prism 8.0 (GraphPad Software, CA, USA). Data were presented as means ± SEM. Comparisons were determined using Student's *t* test or one-way analysis of variance (ANOVA). Statistical significance was set at a P value of <0.05.

Protein docking analysis

In the simulation studies, the tertiary structure of hPXR was collected from Palm Database (PDB) with the entry identifier 1ILH (*36*). The casual force field ff14SB (*37*) was applied for protein description. The protonation states of hPXR residues were carefully assigned according to the predicted pK_a (where K_a is the acid dissociation constant) values that were calculated by the PDB2PQR online server (*38*) or the available information of the previous literature (*36*), from which His^{407} was optimized into Neutral HIS, proton HD1 present (HID) as protonated at the delta position. For the ligand **1a**, geometrical optimization was first carried in Gaussian 16 A03 package (*31*) at level of B3LYP theory (*54*–*56*) with a 6-311G* basis set (*57*). The partial charge was then assigned with the restrainged electrostatic potential (RESP) calculation method (*58*). Atom types and parameters of the bonds, angles, dihedrals, and van der Waals for **1a** were described on the basis of the general AMBER force field (GAFF) force filed (*59*). The initial binding complexes of **1a** with the receptor hPXR were collected from the docking process with the AutoDock Vina module (*60*). The final interaction model was selected on the basis of binding energy (enthalpy) calculation from MD trajectory with Amber16 package (*61*). In the operation of the MD simulation, a total of 2 ns with a 2-fs time step calculation was performed, among which the solvation effects, long-range electrostatic interactions, and bond restriction were described with the transferable interatomic potential with three points (TIP3P) model (*62*), the particle mesh Ewald method (*63*), and the SHAKE algorithm (*64*), respectively. Energy decomposition study was then carried out from the last 1-ns MD trajectory to ensure the necessary equilibrium state.

Supplementary Materials

This PDF file includes:
Supplementary Text
Figs. S1 to S98
Tables S1 to S8

Other Supplementary Material for this manuscript includes the following:
CIF files S1 to S3

View/request a protocol for this paper from *Bio-protocol*.

REFERENCES AND NOTES

1. S. U. Dighe, F. Juliá, A. Luridiana, J. J. Douglas, D. Leonori, A photochemical dehydrogenative strategy for aniline synthesis. *Nature* **584**, 75–81 (2020).
2. K. B. Feng, R. E. Quevedo, J. T. Kohrt, M. S. Oderinde, U. Reilly, M. C. White, Late-stage oxidative C(sp^3)–H methylation. *Nature* **580**, 621–627 (2020).
3. X. H. Zhang, R. T. Smith, C. Le, S. J. McCarver, B. T. Shireman, N. I. Carruthers, D. W. C. MacMillan, Copper-mediated synthesis of drug-like bicyclopentanes. *Nature* **580**, 220–226 (2020).
4. J. He, L. G. Hamann, H. M. L. Davies, R. E. J. Beckwith, Late-stage C-H functionalization of complex alkaloids and drug molecules via intermolecular rhodium-carbenoid insertion. *Nat. Commun.* **6**, 5943 (2015).
5. B. K. Hong, T. P. Luo, X. G. Lei, Late-stage diversification of natural products. *ACS Cent. Sci.* **6**, 622–635 (2020).
6. K. E. Kim, A. N. Kim, C. J. McCormick, B. M. Stoltz, Late-stage diversification: A motivating force in organic synthesis. *J. Am. Chem. Soc.* **143**, 16890–16901 (2021).
7. S. H. Kennedy, B. D. Dherange, K. J. Berger, M. D. Levin, Skeletal editing through direct nitrogen deletion of secondary amines. *Nature* **593**, 223–227 (2021).
8. O. Wagnières, Z. R. Xu, Q. Wang, J. P. Zhu, Unified strategy to monoterpene indole alkaloids: Total syntheses of (±)-goniomitine, (±)-1,2-dehydroaspidospermidine, (±)-aspidospermidine, (±)-vincadifformine, and (±)-kopsihainanine A. *J. Am. Chem. Soc.* **136**, 15102–15108 (2014).
9. L. W. Zeng, Y. X. Lin, J. M. Li, H. Sajiki, H. J. Xie, S. L. Cui, Skeletal reorganization divergence of *N*-sulfonyl ynamides. *Nat. Commun.* **11**, 5639 (2020).
10. N. Rauscher, L. Næsborg, C. Jandl, T. Bach, Concise total synthesis of agarozizanol B via a strained photocascade intermediate. *Angew. Chem. Int. Ed.* **60**, 24039–24042 (2021).
11. X. H. Zeng, D. L. Boger, Total synthesis of (−)-strempeliopine. *J. Am. Chem. Soc.* **143**, 12412–12417 (2021).
12. G. N. Wang, H. Huang, W. G. Guo, C. X. Qian, J. W. Sun, Unusual skeletal reorganization of oxetanes for the synthesis of 1,2-dihydroquinolines. *Angew. Chem. Int. Ed.* **59**, 11245–11249 (2020).
13. M. Skwarczynski, Y. Kiso, Application of the O–N intramolecular acyl migration reaction in medicinal chemistry. *Curr. Med. Chem.* **14**, 2813–2823 (2007).
14. D. Ameen, T. J. Snape, Mechanism and application of Baker–Venkataraman O→C acyl migration reactions. *Synthesis* **47**, 141–158 (2014).
15. C. Jiang, H. Lu, W. H. Xu, J. Wu, T. Y. Yu, P. F. Xu, H. Wei, Ni-catalyzed 1,2-acyl migration reactions triggered by C–C bond activation of ketones. *ACS Catal.* **10**, 1947–1953 (2020).
16. G. Fumagalli, S. Stanton, J. F. Bower, Recent methodologies that exploit C–C single-bond cleavage of strained ring systems by transition metal complexes. *Chem. Rev.* **117**, 9404–9432 (2017).
17. Z. Q. Rong, H. N. Lim, G. Dong, Intramolecular acetyl transfer to olefins by catalytic C–C bond activation of unstrained ketones. *Angew. Chem. Int. Ed.* **57**, 475–479 (2018).
18. M. D. Kärkäs, J. A. Porco Jr., C. R. J. Stephenson, Photochemical approaches to complex chemotypes: Applications in natural product synthesis. *Chem. Rev.* **116**, 9683–9747 (2016).
19. B. K. Hong, W. L. Liu, J. Wang, J. B. Wu, Y. C. Kadonaga, P. J. Cai, H. X. Lou, Z. X. Yu, H. H. Li, X. G. Lei, Photoinduced skeletal rearrangements reveal radical-mediated synthesis of terpenoids. *Chem* **5**, 1671–1681 (2019).
20. J. Oren, M. Vardi, R. Viskin, S. Abramson, B. Fuchs, Homoconjugated ketones with extended unsaturation: Wavelength-selective, regioselective, diastereoselective, and enantiospecific photochemical transformations of methyl 7-oxospiro[5.5]undeca-1,3-and -2,4,-diene-2-carboxylate. *Helv. Chim. Acta* **76**, 1182–1193 (1993).
21. V. Singh, M. Porinchu, Sigmatropic 1,2- and 1,3-acyl shifts in excited states: A novel, general protocol for the synthesis of tricyclopentanoids and protoilludanes. *Tetrahedron* **52**, 7087–7126 (1996).
22. D.-S. Hsu, Y.-Y. Chou, Y.-S. Tung, C.-C. Liao, Photochemistry of tricyclo[5.2.2.$0^{2,6}$]undeca-4,10-dien-8-ones: An efficient general route to substituted linear triquinanes from 2-methoxyphenols. Total synthesis of (±)-$\Delta^{9(12)}$-capnellene. *Chem. A Eur. J.* **16**, 3121–3131 (2010).
23. D. Lübken, B. Siekmeyer, M. Kalesse, Photochemical 1,3-acyl shifts in natural product synthesis. *Eur. J. Org. Chem.* **41**, e202200701 (2022).
24. A. W. Schuppe, D. Huang, Y. F. Chen, T. R. Newhouse, Total synthesis of (−)-xylogranatopyridine B via a palladium-catalyzed oxidative stannylation of enones. *J. Am. Chem. Soc.* **140**, 2062–2066 (2018).
25. A. W. Schuppe, Y. Z. Zhao, Y. N. Liu, T. R. Newhouse, Total synthesis of (+)-granatumine A and related bislactone limonoid alkaloids via a pyran to pyridine interconversion. *J. Am. Chem. Soc.* **141**, 9191–9196 (2019).
26. W. Zhang, Z. Y. Zhang, J. C. Tang, J. T. Che, H. Y. Zhang, J. H. Chen, Z. Yang, Total synthesis of (+)-haperforin G. *J. Am. Chem. Soc.* **142**, 19487–19492 (2020).

27. Q. G. Tan, X. D. Luo, Meliaceous limonoids: Chemistry and biological activities. *Chem. Rev.* **111**, 7437–7522 (2011).
28. J. Luo, Y. P. Sun, Q. R. Li, L. Y. Kong, Research progress of meliaceous limonoids from 2011 to 2021. *Nat. Prod. Rep.* **39**, 1325–1365 (2022).
29. W. S. Li, L. Shen, T. Bruhn, P. Pedpradab, J. Wu, G. Bringmann, Trangmolins A–F with an unprecedented structural plasticity of the rings A and B: New insight into limonoid biosynthesis. *Chem. A Eur. J.* **22**, 11719–11727 (2016).
30. W. S. Li, J. Wu, J. Li, T. Satyanandamurty, L. Shen, G. Bringmann, Krishnadimer A, an axially chiral non-biaryl natural product: Discovery and biomimetic synthesis. *Org. Lett.* **19**, 182–185 (2017).
31. M. J. Frisch, G. W. Trucks, H. B. Schlegel, G. E. Scuseria, M. A. Robb, J. R. Cheeseman, G. Scalmani, V. Barone, G. A. Petersson, H. Nakatsuji, X. Li, M. Caricato, A. V. Marenich, J. Bloino, B. G. Janesko, R. Gomperts, B. Mennucci, H. P. Hratchian, J. V. Ortiz, A. F. Izmaylov, J. L. Sonnenberg, D. Williams-Young, F. Ding, F. Lipparini, F. Egidi, J. Goings, B. Peng, A. Petrone, T. Henderson, D. Ranasinghe, V. G. Zakrzewski, J. Gao, N. Rega, G. Zheng, W. Liang, M. Hada, M. Ehara, K. Toyota, R. Fukuda, J. Hasegawa, M. Ishida, T. Nakajima, Y. Honda, O. Kitao, H. Nakai, T. Vreven, K. Throssell, J. A. Montgomery Jr., J. E. Peralta, F. Ogliaro, M. J. Bearpark, J. J. Heyd, E. N. Brothers, K. N. Kudin, V. N. Staroverov, T. A. Keith, R. Kobayashi, J. Normand, K. Raghavachari, A. P. Rendell, J. C. Burant, S. S. Iyengar, J. Tomasi, M. Cossi, J. M. Millam, M. Klene, C. Adamo, R. Cammi, J. W. Ochterski, R. L. Martin, K. Morokuma, O. Farkas, J. B. Foresman, D. J. Fox, Gaussian 16, Gaussian Inc., Wallingford, CT (2016).
32. Y. Zhao, D. G. Truhlar, The M06 suite of density functionals for main group thermochemistry, thermochemical kinetics, noncovalent interactions, excited states, and transition elements: Two new functionals and systematic testing of four M06-class functionals and 12 other functionals. *Theor. Chem. Acc.* **120**, 215–241 (2008).
33. F. Furche, R. Ahlrichs, Adiabatic time-dependent density functional methods for excited state properties. *J. Chem. Phys.* **117**, 7433–7447 (2002).
34. G. Scalmani, M. J. Frisch, B. Mennucci, J. Tomasi, R. Cammi, V. Barone, Geometries and properties of excited states in the gas phase and in solution: Theory and application of a time-dependent density functional theory polarizable continuum model. *J. Chem. Phys.* **124**, 094107 (2006).
35. J. W. Jonker, C. Liddle, M. Downes, FXR and PXR: Potential therapeutic targets in cholestasis. *J. Steroid Biochem. Mol. Biol.* **130**, 147–158 (2012).
36. R. E. Watkins, G. B. Wisely, L. B. Moore, J. L. Collins, M. H. Lambert, S. P. Williams, T. M. Willson, S. A. Kliewer, M. R. Redinbo, The human nuclear xenobiotic receptor PXR: Structural determinants of directed promiscuity. *Science* **292**, 2329–2333 (2001).
37. J. A. Maier, C. Martinez, K. Kasavajhala, L. Wickstrom, K. E. Hauser, C. Simmerling, ff14SB: Improving the accuracy of protein side chain and backbone parameters from ff99SB. *J. Chem. Theor. Comput.* **11**, 3696–3713 (2015).
38. T. J. Dolinsky, J. E. Nielsen, J. A. McCammon, N. A. Baker, PDB2PQR: An automated pipeline for the setup of Poisson–Boltzmann electrostatics calculations. *Nucleic Acids Res.* **32**, W665–W667 (2004).
39. J. Marrero, A. D. Rodríguez, C. L. Barnes, Intricarene, an unprecedented trispiropentacyclic diterpene from the caribbean sea plume *Pseudopterogorgia kallos*. *Org. Lett.* **7**, 1877–1880 (2005).
40. J. Marrero, A. D. Rodríguez, P. Baran, R. G. Raptis, J. A. Sánchez, E. Ortega-Barria, T. L. Capson, Bielschowskysin, a gorgonian-derived biologically active diterpene with an unprecedented carbon skeleton. *Org. Lett.* **6**, 1661–1664 (2004).
41. R. A. Craig II, B. M. Stoltz, Polycyclic furanobutenolide-derived cembranoid and norcembranoid natural products: Biosynthetic connections and synthetic efforts. *Chem. Rev.* **117**, 7878–7909 (2017).
42. D. Stichnoth, P. Kölle, T. J. Kimbrough, E. Riedle, R. de Vivie-Riedle, D. Trauner, Photochemical formation of intricarene. *Nat. Commun.* **5**, 5597 (2014).
43. P. D. Scesa, L. M. West, S. P. Roche, Role of macrocyclic conformational steering in a kinetic route toward bielschowskysin. *J. Am. Chem. Soc.* **143**, 7566–7577 (2021).
44. A. D. Rodríguez, J. G. Shi, The first cembrane-pseudopterane cycloisomerization. *J. Org. Chem.* **63**, 420–421 (1998).
45. J. Wu, S. Zhang, T. Bruhn, Q. Xiao, H. X. Ding, G. Bringmann, Xylogranatins F–R: Antifeedants from the Chinese mangrove, *Xylocarpus granatum*, a new biogenetic pathway to tetranortriterpenoids. *Chem. A Eur. J.* **14**, 1129–1144 (2008).
46. J. Li, M. Y. Li, T. Bruhn, D. C. G. Götz, Q. Xiao, T. Satyanandamurty, J. Wu, G. Bringmann, Andhraxylocarpins A–E: Structurally intriguing limonoids from the true mangroves *Xylocarpus granatum* and *Xylocarpus moluccensis*. *Chem. A Eur. J.* **18**, 14342–14351 (2012).
47. S. P. Pitre, L. E. Overman, Strategic use of visible-light photoredox catalysis in natural product synthesis. *Chem. Rev.* **122**, 1717–1751 (2022).
48. J. Großkopf, T. Kratz, T. Rigotti, T. Bach, Enantioselective photochemical reactions enabled by triplet energy transfer. *Chem. Rev.* **122**, 1626–1653 (2022).
49. W. S. Li, Z. P. Jiang, L. Shen, P. Pedpradab, T. Bruhn, J. Wu, G. Bringmann, Antiviral limonoids including khayanolides from the Trang mangrove plant *Xylocarpus moluccensis*. *J. Nat. Prod.* **78**, 1570–1578 (2015).
50. J. Z. Zhang, W. S. Li, Y. G. Dai, L. Shen, J. Wu, Twenty-nine new limonoids with skeletal diversity from the mangrove plant, *Xylocarpus moluccensis*. *Mar. Drugs* **16**, 38 (2018).
51. W. S. Li, A. Mándi, J. J. Liu, L. Shen, T. Kurtán, J. Wu, Xylomolones A–D from the Thai mangrove *Xylocarpus moluccensis*: Assignment of absolute stereostructures and unveiling a convergent strategy for limonoid biosynthesis. *J. Org. Chem.* **84**, 2596–2606 (2019).
52. L. Shen, Q. Liao, M. Zhang, J. Wu, Limonoids with diverse structures of rings-A,B from the Thai mangrove, *Xylocarpus moluccensis*. *Fitoterapia* **147**, 104737 (2020).
53. C. Zhou, E. J. Poulton, F. Grun, T. K. Bammler, B. Blumberg, K. E. Thummel, D. L. Eaton, The dietary isothiocyanate sulforaphane is an antagonist of the human steroid and xenobiotic nuclear receptor. *Mol. Pharmacol.* **71**, 220–229 (2007).
54. C. Lee, W. Yang, R. G. Parr, Development of the Colle-Salvetti correlation-energy formula into a functional of the electron density. *Phys. Rev. B Condens. Matter* **37**, 785–789 (1988).
55. A. D. Becke, Density-functional thermochemistry. I. The effect of the exchange-only gradient correction. *J. Chem. Phys.* **96**, 2155–2160 (1992).
56. A. D. Becke, Density-functional thermochemistry. III. The role of exact exchange. *J. Chem. Phys.* **98**, 5648–5652 (1993).
57. R. Krishnan, J. S. Binkley, R. Seeger, J. A. Pople, Self-consistent molecular orbital methods. XX. A basis set for correlated wave functions. *J. Chem. Phys.* **72**, 650 (1980).
58. W. D. Cornell, P. Cieplak, C. I. Bayly, P. A. Kollman, Application of RESP charges to calculate conformational energies, hydrogen bond energies, and free energies of solvation. *J. Am. Chem. Soc.* **115**, 9620–9631 (1993).
59. J. Wang, R. M. Wolf, J. W. Caldwell, P. A. Kollman, D. A. Case, Development and testing of a general amber force field. *J. Comput. Chem.* **25**, 1157–1174 (2004).
60. O. Trott, A. J. Olson, AutoDock Vina: Improving the speed and accuracy of docking with a new scoring function, efficient optimization, and multithreading. *J. Comput. Chem.* **31**, 455–461 (2010).
61. D. A. Case, D. S. Cerutti, I.T.E. Cheatham, T. A. Darden, R. E. Duke, T. J. Giese, H. Gohlke, A. W. Goetz, D. Greene, N. Homeyer, S. Izadi, A. Kovalenko, T. S. Lee, S. LeGrand, P. Li, C. Lin, J. Liu, T. Luchko, R. Luo, D. Mermelstein, K. M. Merz, G. Monard, H. Nguyen, I. Omelyan, A. Onufriev, F. Pan, R. Qi, D. R. Roe, A. Roitberg, C. Sagui, C. L. Simmerling, W. M. Botello-Smith, J. Swails, R. C. Walker, J. Wang, R. M. Wolf, X. Wu, L. Xiao, D. M. York, P. A. Kollman, AMBER 16 (2017).
62. W. L. Jorgensen, J. Chandrasekhar, J. D. Madura, M. L. Klein, Comparison of simple potential functions for simulating liquid water. *J. Chem. Phys.* **79**, 926–935 (1983).
63. U. Essmann, L. Perera, M. L. Berkowitz, T. Darden, H. Lee, L. G. Pedersen, A smooth particle mesh Ewald method. *J. Chem. Phys.* **103**, 8577–8593 (1995).
64. J. P. Ryckaert, G. Ciccotti, H. J. C. Berendsen, Numerical integration of the Cartesian equations of motion of a system with constraints: Molecular dynamics of n-alkanes. *J. Comput. Phys.* **23**, 327–341 (1977).
65. J. C. Zhang, Q. Liao, L. Shen, J. Wu, Twenty-five limonoids from the Hainan mangrove, *Xylocarpus granatum*. *Bioorg. Chem.* **100**, 103903 (2020).

Acknowledgments: We thank P. Pedpradab (Rajamangala University of Technology Srivijaya, Trang Province, Thailand) for providing the mangrove materials used in this work. We thank Z.-H. Xiao, A.-J. Sun, and Y. Zhang (Equipment Public Service Center, South China Sea Institute of Oceanology, Chinese Academy of Sciences) for recording the 700-MHz NMR spectra and HR-ESIMS. **Funding:** This work was supported by Guangdong Basic and Applied Basic Research Foundation, Funds for Distinguished Young Scholar, PR China (2020B1515020056), and the National Natural Science Foundation of China (U20A2001, 31770377, and 81930112). **Author contributions:** Conceptualization: L.S. Methodology: Y.L., X.-C.M., and L.S. Investigation: J.W., S.-J.L., L.J., and X.-C.M. Writing (original draft): J.W., Y.L., S.-J.L., X.-C.M., and L.S. Writing (review and editing): J.W., Y.L., X.-C.M., and L.S. Funding acquisition: J.W., Y.L., X.-C.M., and L.S. Resources: J.W., Y.L., X.-C.M., and L.S. Supervision: Y.L., X.-C.M., and L.S. **Competing interests:** The authors declare that they have no competing interests. **Data and materials availability:** All data needed to evaluate the conclusions in the paper are present in the paper and/or the Supplementary Materials.

Submitted 9 August 2022
Accepted 29 December 2022
Published 27 January 2023
10.1126/sciadv.ade2981